J. Condensed Matter Nucl. Sci. 29 (2019) 416–439

Research Article

Investigation of Electron Mediated Nuclear Reactions

Andras Kovacs* and Dawei Wang

Fiskarsin Voima Oy, Nordanvik 142, 02580 Sjundeå, Finland

Pavel N. Ivanov

Moscow Engineering Physics Institute, Kashirskoe shosse 31, Moscow, 115409 Russia

Abstract

We investigated the concept of electron mediated nuclear reactions. The analysis of experimental reaction data indicates burst-like reactions and continuous energy production phases, which appear to be two distinct processes. We discuss the signatures of electron states which are highly localized around the nucleus. A theory of electron transitions into such highly localized states is proposed, with good correspondence to the observed reaction dynamics. Understanding the underlying nuclear reaction requires further investigation. With respect to applications, the discovered process implies the possibility of sustainable energy production from fuels comprising hydrogen, nickel, and lithium.
 ISSN 2227-3123

Keywords: Electron zitterbewegung, Highly localized electron states, Nuclear fuel, Nuclear energy production

1. Introduction

Up to now, an elementary particle intermediated nuclear reaction process has been conceptualized and investigated only in the context of neutron-mediated reaction of heavy nuclei. Here, we investigate the concept of electron mediated nuclear reactions. This class of nuclear reactions appears to involve an electron–nucleus configuration where the electron and the nucleus are in close proximity, and the reaction generates energetic electrons.

In this paper, we discuss Ni containing materials as possible fuels for electron mediated nuclear reactions. Observation of nuclear energy production from nickel–hydrogen and nickel–deuterium systems has been well established in multiple experiments [1–4]. In a previous publication [4], we have described experiments with Ni and Li containing mixtures, that showed experimental evidence of an exothermic nuclear reaction, which appears to be a continuous and well controllable reaction process. However, the theory of such reaction process is not yet settled. By focusing on the role of excited electron states in these experiments, we expect to progress towards uncovering the underlying reaction process.

*Corresponding author. E-mail: andras.kovacs@broadbit.com.

 ISSN 2227-3123

This paper is organized as follows. In Section 2, we discuss the experimental signatures of electron-mediated nuclear reaction processes with nickel containing fuels. In Section 3, we discuss in detail the possibility of highly localized electron states where an electron orbits a proton or deuteron at 0.383 pm proximity. Conclusions are drawn in Section 4.

2. Analysis of Nickel Fueled Reactor Experiments

Previous nickel fuel related observations of exothermic nuclear energy production also involved the presence of hydrogen [1,2,5], deuterium [3,8], or aqueous electrolysis [19]; therefore, the general assumption was that some type of hydrogen or deuterium involving fusion reaction plays a role in the underlying nuclear process. We have investigated lithium–nickel–copper containing fuel mixtures as possible fuels for electron mediated nuclear reactions [4], and we showed experimental evidence for an exothermic nuclear reaction. In our setup, hydrogen was introduced in the form of LiOH, produced over lithium during the assembly and sealing of fuel containers in ambient air. In the near future we plan to perform a LiOH-free counter-experiment in order to be certain that hydrogen plays a role in the initiation of this nuclear reaction.

As documented in [4], the observed reaction is initially a sequence of sudden heat and radiation producing bursts, which we are able to periodically re-initiate by temperature cycling. Figure 6 highlights some sudden temperature jumps. We note that the bursts appear to have originated from the lithium-rich molten phase. Such bursts imply chain reaction-like reaction dynamics. The observed bursts had varying strength and duration, and the measured exothermic heat production has been several hundred Watts. During a strong burst in our experiment, we observed radio-frequency signal generation with uniform power spreading in the 1–10 MHz frequency range; such flat radio-frequency power spectrum is an expected signature of decelerating charged particles. At the same time, a Geiger counter placed 0.5 m from the fuel container indicated a radiation level 40 times that of the background.

In [6], the gamma spectrum was monitored during the heating of Ni and $LiAlH_4$ fuel mixture, at similar temperature conditions as in our experiment. In that experiment, at a certain point, a strong burst event occurred whose gamma radiation spectrum is shown in Fig. 1, with the red dots indicating the signal of interest. The overall signal-to-background count ratio is 5.44. Because of the similar experimental conditions and the transient (i.e. burst-like) radiation, we anticipate that the gamma spectrum shown in [6] has the same origin as in our experiment.

Such bursty reaction dynamics was also observed in Ni–H and Ni–D systems, in the initial experimental phase. Figure 7 of Ref. [8] shows intense heat-producing bursts during the heat treatment of both Ni–H and Ni–D fuels. Based on continuous monitoring of H and D gas pressure, the authors conclude that the energy production during these bursts is too high for any possible chemical process. Figure 6 of Ref. [16] shows heat-producing bursts during the gas treatment of Ni–H fuel, as well as the coincident burst-like pressure increases. These burst type processes may be signatures of the same underlying nuclear reaction.

Several experiments achieved continuous energy production from Ni–H [1,2] and Ni–D [3] fuels. The contrast between the bursty and continuous reaction dynamics is shown in Fig. 2. A careful measurement of the radiation spectrum during continuous Ni–H energy production process [1] shows the absence of any measurable radiation signal above 100 keV. In a nickel electrolysis experiment, the observation of low-level X-ray emission in the 20 keV energy range and lasting several months after the experiment has been reported 19. Therefore, the bursty and continuous nuclear processes can be distinguished both through the different reaction dynamics and different gamma spectrum. However, occasional spontaneous overheating of copper–nickel alloy wires during Ni–H energy production runs has also been reported in [2]. Such sudden overheating indicates possible transitions between a continuous energy production process and the initial bursty reaction process.

It is useful to analyze in detail the transition from a bursty process into a continuous process, which has also been observed in detail in our experiments. Figure 21 of Ref. [4] shows the overall temperature evolution during

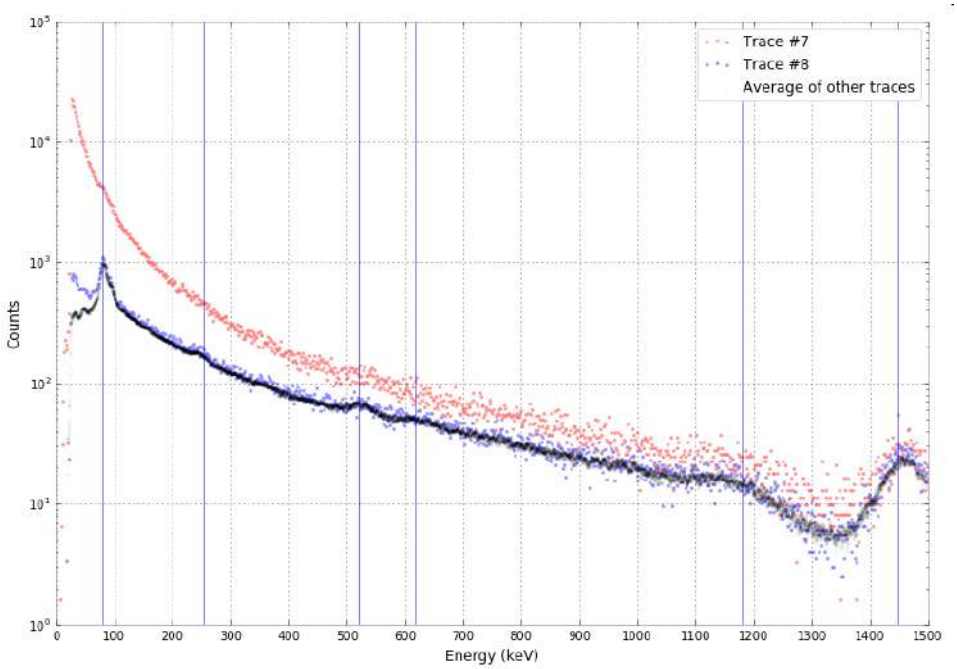

Figure 1. The gamma spectrum measurement of a burst from Ni+$LiAlH_4$ fuel during heating, produced by the authors of [6].

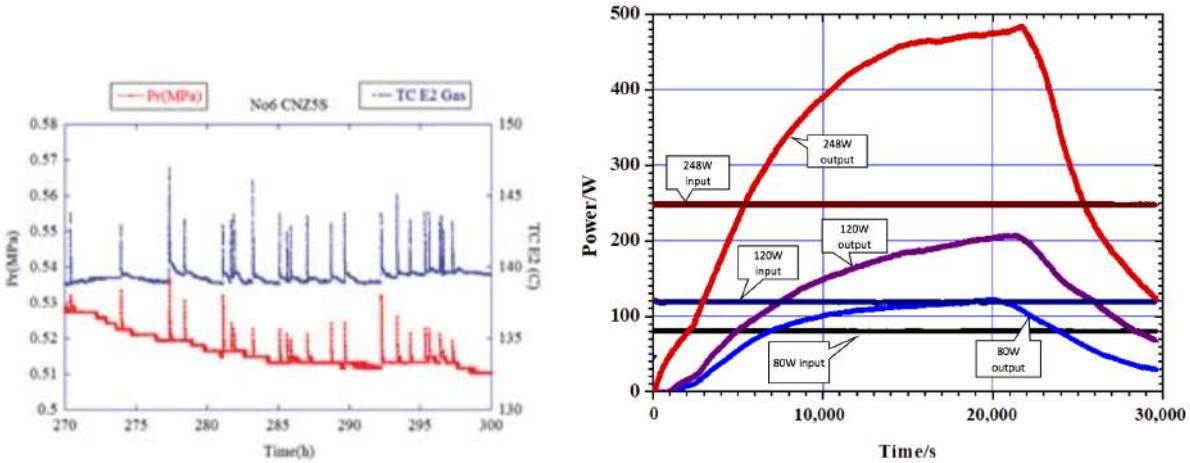

(**a**) (**b**)

Figure 2. The contrast between bursty (*left*), reproduced from [16]) and continuous (*right*), reproduced from [3]) reaction dynamics with nickel based fuel.

this process. After about half an hour at the operating temperature regime, the continuous reaction starts up and is maintained for approximately three hours. Figure 3 shows the temperature evolution of the heating and cooling phases

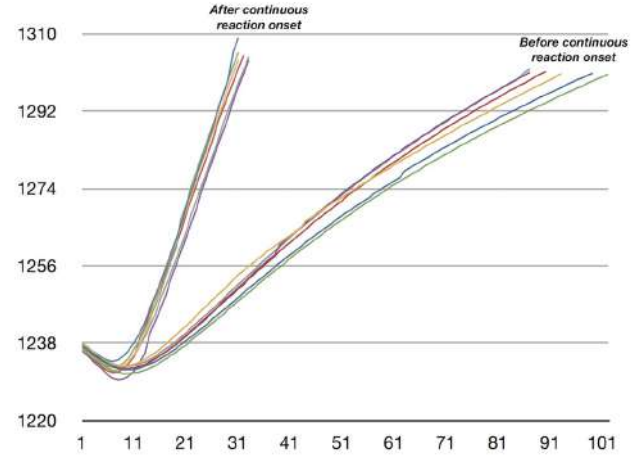

(**a**)

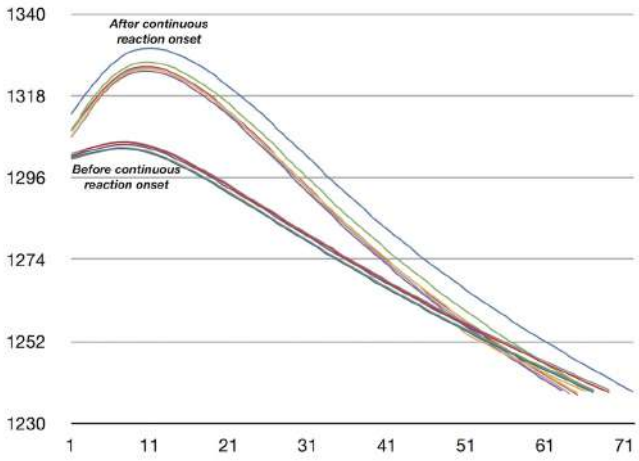

(**b**)

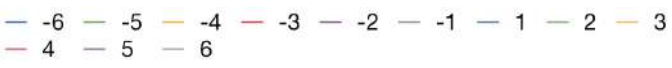

(**c**)

Figure 3. Temperature (°C) vs. time (s) charts during transition from bursty to continuous process with Ni–Cu–Li fuel mixture. (a) heating phases (constant heating power). (b) Cooling phases (zero heating power). The labels (c) indicate cycle no. relative to the starting of continuous reaction.

in the six cycles before and after the continuous reaction start-up. The negative (vs. positive) numbers of labels indicate cycle numbers before (vs. after) the starting of continuous reaction.

The continuous reaction starts up right away at the beginning of a certain heating cycle (i.e. "cycle 1"), as can be seen from the steeper slope already at the beginning. The fairly constant slope during the heating cycles, as well as the very similar slope among the positive numbered cycles show that the reaction produces constant exothermic power during the heating cycles. Signatures of the burst-like reaction (i.e. sudden temperature jumps) can be seen in some negative numbered preceding cycles, and also simultaneously with the continuous reaction in some positive numbered cycles. Cycles 1, 2, and 5 show very visible temperature jumps. In the cooling phase, the first observable feature is a temperature overshoot in the positive numbered cycles, relative to the temperature evolution of the negative numbered cycles. This indicates that the continuous reaction stays active for some seconds after the heating shut-off. Subsequently, the cooling rate is somewhat faster in the positive numbered cycles than in the negative numbered cycles. This is the consequence of local heat generation during the continuous reaction, which was picked up by the nearby thermocouple. It means that the average reactor temperature at the end of heating is somewhat lower in the positive numbered cycles than in the negative numbered cycles, because the electric heating was turned on for a much shorter time. The dynamics of the temperature falling phase indicates little or no exothermic reaction occurring during the temperature fall. Therefore, the reaction dynamics is actually semi-continuous, i.e. the continuous exothermic power is present mainly during the heating phases.

The longer-term dynamics of this continuous reaction was analyzed by constructing the frequency spectrum of the temperature signal's autocorrelation function. Figure 4 shows this spectrum for the initial part of the operating temperature regime, over the 20 minutes segment prior to the semi-continuous reaction onset, and then the spectrum for the duration of a semi-continuous exothermic reaction. The top part of Fig. 4 has less sharp auto-correlation peaks, even though the transients at the start of operating temperature regime were excluded. This may be partly caused by remaining transients of the initial operating temperature regime, and partly caused by the bursty temperature jumps in the initial phase. The continuous reaction part shows very sharp auto-correlation peaks and the absence of high-frequency noise. Since the heating program is controlled via temperature feedback, this data proves that the reaction dynamics are highly ordered, and remain nearly constant from cycle to cycle. There must be some reaction control parameter, which regulates the reaction rate to such a constant value. Perhaps the rate of nickel influx into the molten phase is such a control parameter. In summary, we have shown that the exothermic nuclear reaction of nickel-fueled reactors appears to be electron-mediated. In the initial phases it is a burst-like process, and may subsequently transition into a continuous reaction process, which is highly controllable. It is clearly seen from the data that the initial reaction bursts are a distinct process from the subsequent semi-continuous reaction process.

We also investigated a lithium-nickel-aluminum fuel composition, enclosed in a welded stainless steel container. The approximate Li:Ni:Al atomic composition was $1:10:1$. Figure 5 shows the temperature evolution at the fuel container (green curve) and at the edge of reactor (yellow curve), as well as the heating power evolution (blue curve). The horizontal axis shows the elapsed experiment time (seconds); after a slow temperature ramp-up, the left edge of the figure corresponds to the start of a constant 1350°C temperature program. The thermocouple at the fuel container is used for the temperature feedback control. Initially, the heating power is gradually reduced as the reactor transitions from being heated up to maintaining the target temperature. The first vertical dashed line indicates the first reaction signature, which slightly raises the reactor temperature while the heating power is reduced. The next vertical dashed line indicates the second reaction signature, which further raises the reactor temperature while the heating power is even faster reduced. The falling heating power is corroborated by the falling temperature at the edge of the reactor. A run-away reaction has occurred shortly after the red dashed line, which has melted down a large segment of the stainless steel container and destroyed the heating wires. The overall dynamics of this run-away reaction is very similar to the bursty reactions documented in [4], and the presence of electromagnetic emissions has also been detected. In the context of the previously published Li–Ni–Cu fueled experiments, this Li–Ni–Al experiment indicates that the active

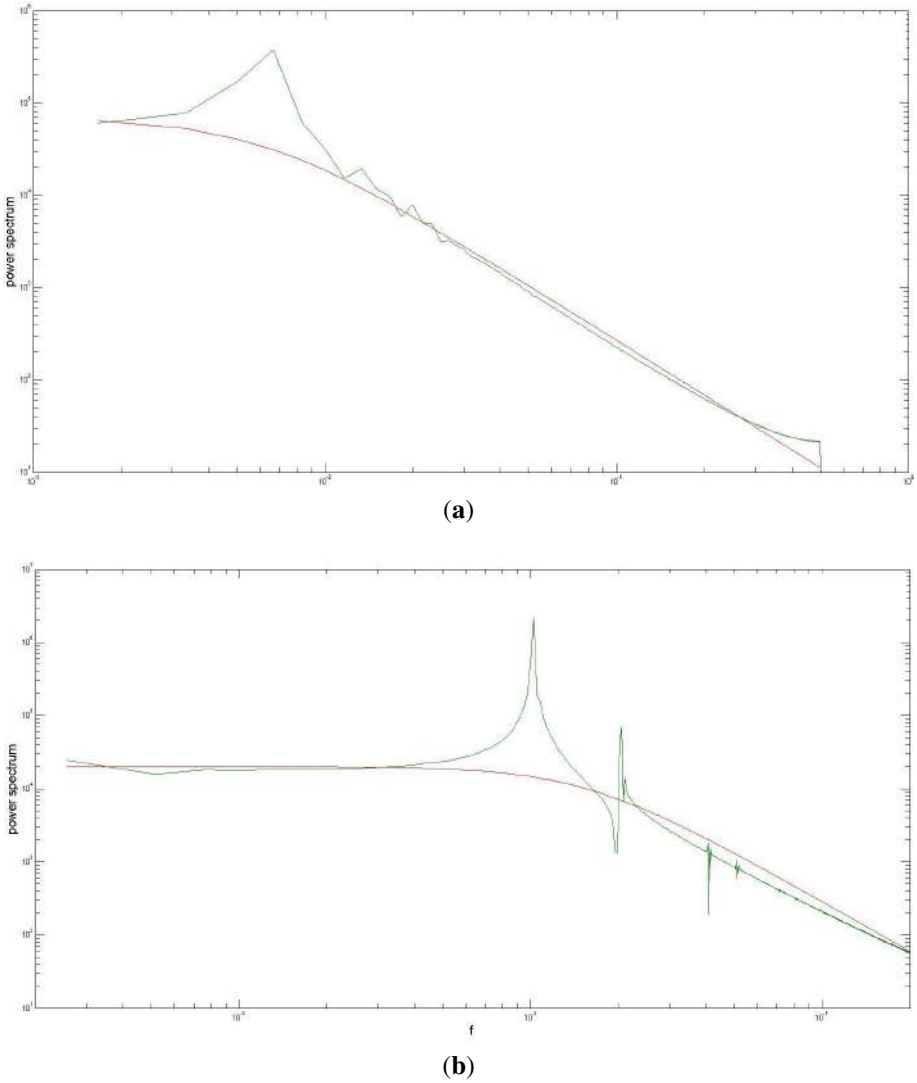

Figure 4. Autocorrelation frequency spectrum during the continuous reaction process with Ni–Cu–Li fuel mixture. (a) The spectrum prior to the continuous reaction and (b) the spectrum during the continuous reaction.

fuel component is indeed nickel and/or lithium.

In the Li–Ni–Cu experiments, the reaction is observed starting from the 1200°C limit (as shown in Fig. 6), which corresponds to the lowest melting temperature of the employed Constantan alloy. In the Li–Ni–Al experiments, the reaction is observed starting from the 1350°C temperature limit (as shown in Fig. 5); this corresponds to the melting temperature of the $AlNi_3$ phase, which is the lowest melting point phase within the nickel-rich nickel–aluminum alloys.

We noted in our experiments, that heating the fuel above approximately 1200°C is accompanied by electromagnetic noise while the temperature is rising. Many thermocouple-sensed electromagnetic disturbances reported in [4] are

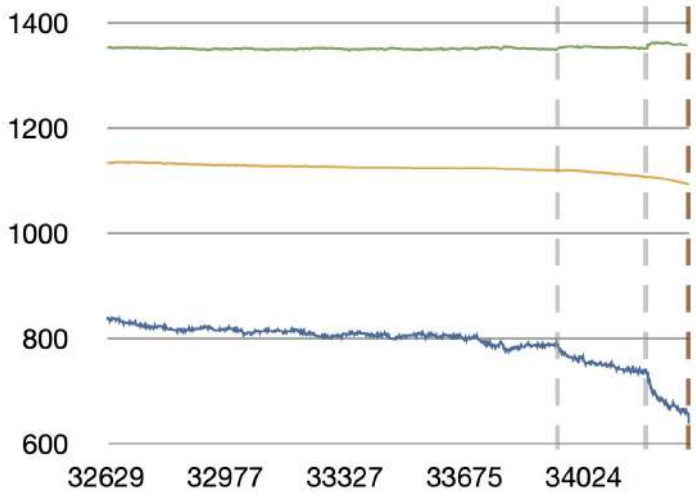

Figure 5. Temperature and heating power evolution of a reactor containing Li–Ni–Al fuel composition. The green curve shows the temperature (°C) at the fuel container, the yellow curve shows the temperature (°C) at the edge of reactor, and the blue curve shows the applied heating power (W). The horizontal axis indicates the elapsed time (s).

therefore not yet attributes of the actual reaction signal, but presumably signatures of such noise generating events. Figure 6, which is adapted from [4], shows the distinction between such non-exothermic precursor events and actual exothermic reaction signatures. The non-exothermic nature of these noise generating events can be seen from the constant slope of the temperature rise. We emphasize that such noise has been absent from calibration runs in the same temperature regime, and is therefore a genuine electromagnetic emission signal of the fuel sample.

As reported in [4], the reaction onset has been very predictable throughout multiple experimental runs, without any excessive waiting times. It requires further studies to determine whether the noise generating events, the sudden reaction bursts, and the continuous reaction processes are precursor events to each other or independent phenomena.

3. Discussion

For the possibility of electron-mediated nuclear reactions, the challenge is to identify the electron configuration which allows much stronger electron–nucleus interaction than the ordinary interaction between the inner shell electrons and the nucleus. It is indeed known that the electron environment can impact, e.g., the rate of nuclear electron capture; this effect has been most extensively studied for ^{7}Be. For instance, Table I. of Ref. [9] shows the half-life ^{7}Be in different environments, where the electron capture rate of ^{7}Be can indeed be changed by its environment. An electron configuration involving close electron–nucleus proximity would enhance the probability of electron capture. Most importantly, a close proximity electron–proton or electron–deuteron configuration would allow small inter-nuclei distance between such quasi-neutron and some other nucleus, thereby enabling catalyzed fusion reactions.

A mechanism for high probability nucleus-to-electron energy transfer is a pre-condition for the production of energetic electrons, which produce the observed braking signatures. In muon-catalyzed p–D fusion experiments, it has been observed that the muon carries away the fusion energy in most reactions, suggesting that a similar effect might arise under close electron–nucleus proximity. Until recently, no similar effect has been observed with electrons. However, it was recently observed that certain environments cause a shift in the de-excitation pathway of a fused

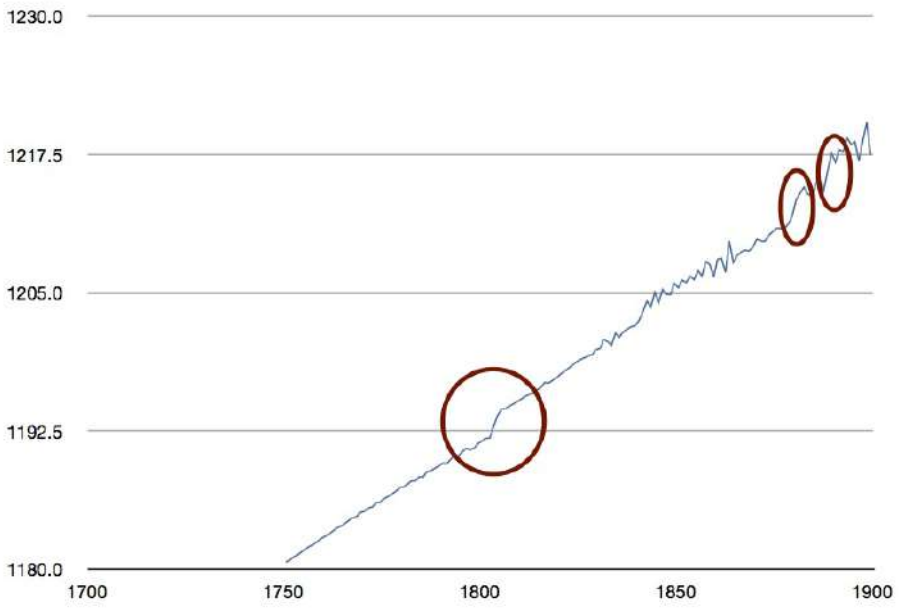

Figure 6. Temperature (°C) vs. time (s) measurement, reproduced from [4]. The rapid exothermic events are indicated by red circles. Electromagnetic emissions from non-exothermic processes, which appear as noise, are observable in-between.

^{3}He nucleus from gamma photon emission towards electron acceleration [7]. Specifically, all of the nuclear reaction energy of some p-D fusion events has been carried away by energetic electrons. The results presented in [7] therefore point to the existence of a very special configuration with close electron-nucleus proximity, resulting in strong enough electron–nucleus interaction for electrons to carry away the nuclear excitation energy.

Based on the above motivation, we introduce the idea of excited electron states, where electrons are in very close proximity around the nucleus. Usually, the excitation of electrons results in more delocalization, as electrons are pushed into higher energy orbitals. For the electron to be in a highly excited and highly localized state, the nature of excitation must be different from ordinary orbital excitations. We present below a discussion of such electron transition process.

3.1. Concept of close proximity electron–nucleus configurations

Our investigation of highly localized electron configuration is based on the relativistic quantum physics of the electron. The suggestion of a ring-shaped circulating electron structure has been originally made in 1915 by A. Parson. Such toroidal current structure is characterized by the electron's anapole moment (also referred to as toroidal moment) and charge radius parameters. The relativistic quantum mechanics-based calculation of the electron's toroidal current loop radius and charge radius is generally referred to as the electron's "zitterbewegung". Since Schrödinger's first zitterbewegung calculations in 1930, this structure was studied by many researchers of stochastic electrodynamics; a recent summary of the electron's relativistic dynamics is published in [10]. A quantum field theory based approach for calculating a gauge invariant expression for the electron's anapole moment and charge radius has been published in [11]; this study shows that the electron's zitterbewegung can also be derived through quantum field theory. The

toroidal electron structure is sketched in Fig. 7; the electron current is circulating in both toroidal and poloidal directions, and the electron is locally moving at the speed of light. This light-speed movement of electromagnetic fields around the circulation axes is the electron's wave-like aspect; it is described by the electromagnetic wave equation. The displacement of electromagnetic fields into the orthogonal direction to this toroidal plane is the electron's particle-like aspect; it is described by the equations of relativistic particle dynamic, i.e. the Dirac equation. Reference [10] discusses the connection between these two aspects; i.e. it shows how relativistic particle dynamics arises from the wave-like electromagnetic current loop. We recommend that the reader becomes familiar with zitterbewegung related concepts described in [10], and validates that the presently discussed toroidal wave-like electron aspect is complementing the electron's particle-like dynamics, which is described by the Dirac equation. To avoid misunderstandings in the following paragraphs, we advise the reader to consider this wave-particle duality of the electron structure; i.e. the complementary roles of the electromagnetic wave equation describing electron oscillations within the toroidal zitterbewegung plane, and of the Dirac equation which describes many orders of magnitude slower quantum mechanical oscillations in the perpendicular direction to the zitterbewegung plane. In this study, we work with the virial theorem, which remains valid for the expectation values even in the quantum regime. When we refer to "orbit radius R", we mean its expectation value.

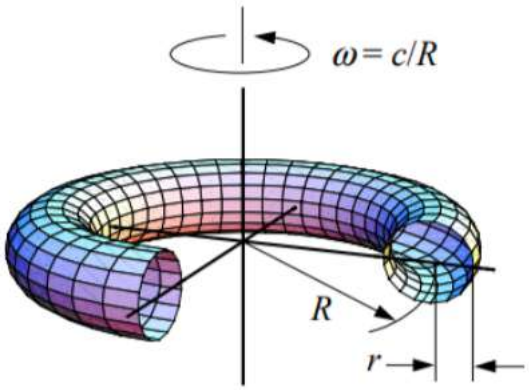

Figure 7. Visualization of the toroidal electron structure. R is the reduced Compton wavelength, and r is the charge radius.

At the thermal energy scale, the presence of electron zitterbewegung is revealed only by magnetic fields which cause a precession of its wave-like current loop circulation; this effect is detected as the electron spin [10], and in spectroscopy it is known as the Zeeman effect. Through the Zeeman effect, a signature of the toroidal electron structure has been experimentally observed for over 100 years, but for most of these years its origin was simply treated as an "inherent property" of the electron. As the electron energy level increases, it's dynamics must eventually be described relativistically, considering both particle-like mechanical motion and wave-like current loop motion. In the following paragraphs we investigate the dynamics of the electron at the reduced Compton wavelength scale, and consider whether it is possible for the electron to have a stable state at such distance around a proton. We refer to this hypothetical state as the "zitterbewegung orbit", and in this context the word "orbit" refers to both particle-like and wave-like motions of the electron charge. When an electron ring is located around a proton at the reduced Compton wavelength radius of $R_0 = 0.38616$ pm, its electrostatic potential is $U_{\text{p0}} = -3.728$ keV. Before falling into the proton's electrostatic potential well, the total electron energy is denoted as E_{total}. The initial energy of the electromagnetic field corresponding to the

electron's wave-like motion is $W_{\text{em0}} = 510.999$ keV.

At an orbit radius R around the proton, the potential energy is $U_{\text{p}} = U_{\text{p0}}(R_0/R)$ and the electromagnetic field energy of purely wave-like motion is $W_{\text{em}} = W_{\text{em0}}(R_0/R)$. For the magnetic field, this relation directly follows from the formula derived in [10]; $W_{\text{magnetic}} = (\hbar v_{\text{wave}}/2R)$. Since the magnetic and electric field energies of the electron's wave-like motion are equal, the same relation holds for the electric field energy. It is seen from this equation that it requires large energy to compress the electron into smaller orbit than R_0. When the electron is in the state of purely wave-like circulation at an orbit radius R, the following energy balance equation holds:

$$W_{\text{em}} - W_{\text{em}\,0} = E_{\text{total}} - U_{\text{p}}. \tag{1}$$

Based on the principle of particle-wave duality, in an equilibrium state we require an equivalence between a purely wave-like zitterbewegung motion, and a simultaneous wave-like zitterbewegung plus relativistic particle-like motion. This equivalence means that in both cases the electron has the same orbit and its zitterbewegung stays centered around the nucleus. In the first case, the wave-like motion has an instantaneous speed vector $\vec{c}_{\text{em}}$, while in the latter case there are two orthogonal instantaneous speed vectors: the wave-like $\vec{v}_{\text{wave}}$ and the particle-like $\vec{v}_{\text{kinetic}}$, with $c^2 = v_{\text{wave}}^2 + v_{\text{kinetic}}^2$. The two descriptions yield the same trajectory if $\vec{c}_{\text{em}} = \vec{v}_{\text{wave}} + \vec{v}_{\text{kinetic}}$ always holds true. An other way to express this equivalence is to require that upon reaching orbit radius R, the electron's particle-like rotation plus zitterbewegung rotation must be equal to a purely wave-like zitterbewegung rotation; i.e. the two descriptions become indistinguishable as the electron establishes an equilibrium state. Figure 8 illustrates the equivalence between these two descriptions of the electron.

Since the electron is at a steady distance R from the proton, and moves at

$$\gamma = \frac{1}{\sqrt{1 - \frac{v^2}{c^2}}},$$

the relativistic formulation of the virial theorem applies to its particle-like motion:

$$E_{\text{kinetic}} = -U_{\text{p}} \frac{\gamma}{\gamma + 1}. \tag{2}$$

The above formula is derived from the relativistic expression of the virial term: $\frac{1}{2}pv = \frac{1}{2}\beta\gamma m_0 c \cdot \beta c$. Considering that

$$E_{\text{kinetic}} = (\gamma - 1)m_0 c^2,$$

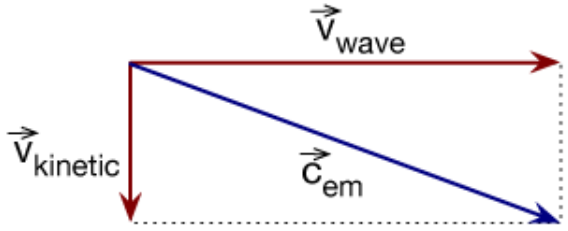

Figure 8. Illustration of the equivalence between instantaneous electron speed vectors in the case of purely wave-like zitterbewegung rotation (*blue*) and the particle-like case of composition between mechanical plus wave-like zitterbewegung rotations (*red*).

we get

$$\frac{1}{2}pv = \frac{\gamma+1}{2\gamma}E_{\text{kinetic}},$$

from which the above formula is derived. Formula (2) is valid for a motion along a straight line. The electromagnetic field energy of the complementing wave-like zitterbewegung current loop is

$$W_{\text{wave}} = W_{\text{em}}\frac{v_{\text{wave}}}{c}. \tag{3}$$

The total energy difference between a purely wave-like state and a wave-like plus relativistic particle-like state is

$$\Delta E = W_{\text{wave}} + E_{\text{kinetic}} - W_{\text{em}}. \tag{4}$$

Equation (2) cannot yet be exact, because it is applicable only to movements along straight line, while the particle-like electron motion is along a circular orbit. We therefore refine Eq. (2) by taking into account also the Thomas precession effect, which causes the circular orbit's angular speed to change as $\omega \to \gamma\omega$ in the frame of the electron. If the proton could be suddenly removed, the electron would continue its path along a straight line, without any instantaneous change of its momentum or kinetic energy with respect to the lab frame. However, its lab frame speed would instantaneously change because of the removal of Thomas precession. Let γ and β describe the electron's Lorentz factor and light speed fraction obtained according to Eq. (2). As discussed above, the Thomas precession effect does not change the electron's momentum or kinetic energy, therefore $p = \beta\gamma m_0 c$ and $E_{\text{kinetic}} = (\gamma-1)m_0c^2$ However, since the electron precesses γ times faster in its own frame than in the lab frame, its lab frame speed becomes $v = \frac{\beta c}{\gamma}$. Using these formulas for p, v, and E_{kinetic}, the following refined kinetic energy formula is obtained from the relativistic formulation of the virial theorem:

$$E_{\text{kinetic}} = -U_{\text{p}}\frac{\gamma^2}{\gamma+1}. \tag{5}$$

Figure 9 shows E_{total} and ΔE as a function of R, calculated from Eqs. (3)–(5). Based on the above stated wave-particle equivalence, we require $\Delta E = 0$. Why is $\Delta E = 0$ in an equilibrium state? The meaning of an equilibrium state is that small perturbations around the equilibrium do not change the energy of the system, e.g. like gravitational energy equilibrium at the top of a hill or in the bottom of a valley. The electron's particle-like aspect is its movement in perpendicular direction to the zitterbewegung plane. The $\Delta E = 0$ condition means that small perturbations of the zitterbewegung orbit state do not change the energy of the system.

This $\Delta E = 0$ condition is met at a negative binding energy, i.e. $E_{\text{total}} > 0$. We note the interesting coincidence that the zitterbewegung radius has shrinked from its natural reduced Compton wavelength value by exactly one electron charge radius; i.e. by 2.82 fm. So far in this analysis, we have neglected the magnetic electron-nucleus interactions. The following refined calculation considers the also Lorentz force experienced by the electron due to the proton's magnetic field.

To minimize the magnetic potential, the electron's and proton's magnetic moments align their directions. Consequently, the proton's magnetic moment is perpendicular to the zitterbewegung plane. The proton-originating magnetic field experienced by the electron is therefore also perpendicular to the zitterbewegung plane, and has the following magnitude:

$$B = \frac{\mu_0}{4\pi}\frac{\mu_{\text{p}}}{R^3} = 2.5\times10^4\ \text{T}.$$

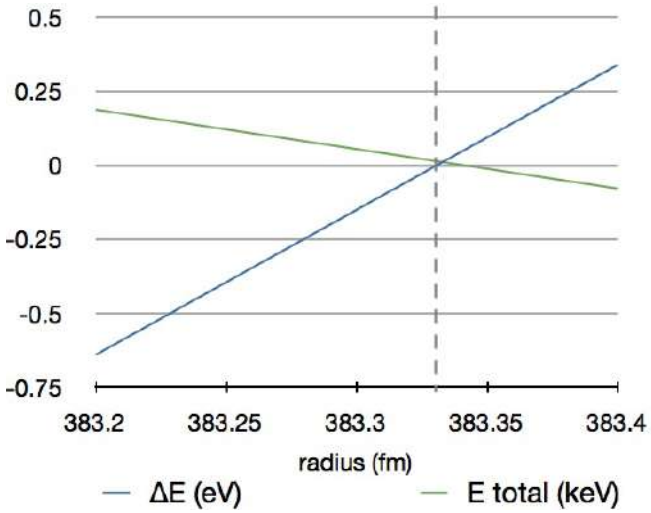

Figure 9. Relativistic estimation of ΔE and E_{total} as a function of the orbit radius. The dashed line indicates the equilibrium condition of $\Delta E = 0$.

The above discussed electrostatic estimation of the equilibrium state gives $\beta = 0.08558$. The Lorentz force experienced by the electron is radial, and has a magnitude of $F_{\text{L}} = ec\beta B = 1.028 \times 10^{-7}$ N. The radial Coulomb force experienced by the electron is

$$F_{\text{C}} = \frac{-U_{\text{p}}}{R} = 1.57 \times 10^{-3}\ \text{N},$$

which is four orders of magnitude larger than the magnetic force. Although the virial theorem is not applicable to a magnetic potential, since the magnetic force is so much smaller than the electrostatic force, and since the two forces are parallel, the magnetic effect can be treated as a linear perturbation of the electric potential. The effective force felt by the electron is $F = F_{\text{C}} + F_{\text{L}} = (1 + 6.55 \times 10^{-5}) \times F_{\text{C}}$. Equating the radial force with the radial derivative of potentials, we get

$$F_{\text{C}} = \frac{-1}{R} U_{\text{p}} \quad \text{and} \quad F_{\text{L}} = \frac{-2}{R} U_{\text{M}}.$$

Therefore at a given radius $F_{\text{L}}/F_{\text{C}} = 2U_{\text{M}}/U_{\text{p}}$. In other words, there needs to be twice as much Coulomb potential as magnetic potential in order to have the same force effect. Using linear perturbation, this additional force can be incorporated into Eq. (5) by making $U_{\text{p}} \rightarrow (1 + 2 \times 6.55 \times 10^{-5}) \times U_{\text{p}}$ substitution. Considering that in the above estimation $U_{\text{p}} = -3.756$ keV, this additional force effect corresponds to $\Delta U_{\text{p}} = 0.49$ eV.

Figure 10 shows the E_{total} and ΔE values obtained after also taking into account the Lorentz force effect, calculated again from Eqs. (3) and (4), and the $U_{\text{p}} \rightarrow U_{\text{p}} + 0.49$ eV adjusted Eq. (5). The $\Delta E = 0$ condition is met at $E_{\text{total}} = 81$ eV. This energy value is our final theoretical estimation for the required transition-initiating electron kinetic energy in case of a proton nucleus.

The obtained result shows that the required transition-initiating electron kinetic energy depends on the nuclear magnetic moment. The deuteron's magnetic moment is 0.857 nuclear magnetons, which is significantly weaker than

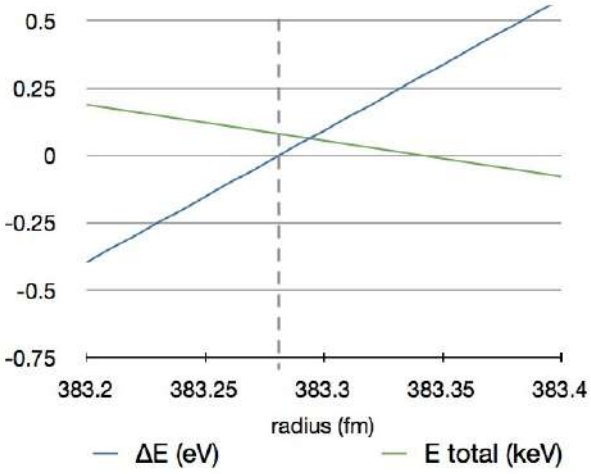

Figure 10. Final estimation of ΔE and E_{total} as a function of the electron orbit radius around a proton, taking into account both electric and magnetic interactions. The broken line indicates the equilibrium condition of $\Delta E = 0$.

the proton's magnetic field. Using this magnetic moment value for the equilibrium state calculation, we obtain $\Delta U_{\text{p}} = 0.15$ eV and $E_{\text{total}} = 35$ eV total energy for a zitterbewegung orbit around a deuteron.

In the preceding paragraphs we refined the total energy estimation by also taking into account the effect of the proton's magnetic field on the electron orbit. In this paragraph we consider how the electron's magnetic field effects the proton in the center. The strong induced magnetic field at the center of the electron orbit interacts with the proton's zitterbewegung motion, causing it to precess around the magnetic field lines. This type of nuclear precession is equivalent to the electron precession described in Section 3.2 of [10], and is routinely exploited in nuclear magnetic resonance imaging devices; this precession frequency is half of the photon frequency causing nuclear magnetic resonance at a given magnetic field strength. The induced precession of the proton's zitterbewegung motion is causing a Zeeman split in the proton's energy levels, and the proton assumes the lower energy level. This lowered proton energy level creates a restoring force for maintaining the equilibrium state; i.e. the electron's zitterbewegung orbit is now a magnetically stabilized meta-stable state. Figure [11] illustrates the closely bound electron–proton system in such zitterbewegung orbit state. This analysis shows that there is a meta-stable equilibrium electron orbit around a proton at the reduced Compton wavelength distance scale, but it has a positive total energy. We emphasize that the positive total energy of this zitterbewegung orbit state implies that at ordinary temperatures electrons occupy the lower energy Bohr orbit state around a proton, where $E_{\text{total}} = -13.6$ eV.

The electron's meta-stable zitterbewegung orbit around a proton, or other light nucleus, may be understood as a fundamental relativistic state. Furthermore, [10] discusses the compatibility between the photon-like zitterbewegung motion and the Heisenberg uncertainty principle. We therefore propose that at a certain electron kinetic energy level the electron's zitterbewegung motion may localize itself as a relativistic orbit around a light nucleus. In case of a proton, our theoretical estimation gives $\approx$80 eV for the transition-initiating electron kinetic energy level, while for the deuteron we obtain $\approx$35 eV energy level. This proposition allows us to correctly predict the reaction dynamics of nickel-fueled reactors. Using relevant experimental data, in the following sections we will precisely identify this required electron kinetic energy level.

Regarding the probability of energetic electron output vs. γ photon output upon nuclear de-excitation, the impact of zitterbewegung orbit presence may be estimated through the methodology shown in [27], specifically through the

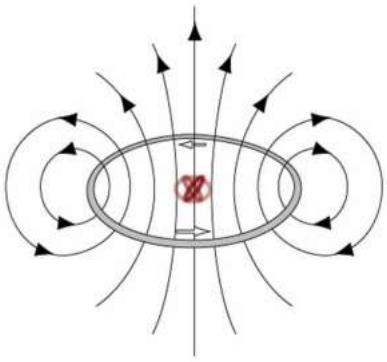

Figure 11. Illustration of the stabilized electron orbit. The gray ring represents the electron's zitterbewegung orbit, the arrows represent magnetic field lines, and the red rings represent the proton's precessing zitterbewegung motion.

precise evaluation of formulas (8)–(11) presented in [27].

Reference [18] reports 2.3 pm inter-nuclei distance measurement in dense states of hydrogen. As discussed in [10], such bond distance is obtained when the zitterbewegung orbits of electrons around neighboring nuclei are phase coherent, and thereby provides further experimental support to our concept of localized zitterbewegung orbit.

Regarding nuclei with $Z > 1$, we note that for ^{4}He such state would not be stable because it has no nuclear magnetic moment. In case of lithium, our theoretical estimation gives approximately 150 eV for the required electron kinetic energy level. However, the presence of a zitterbewegung orbit electron around a lithium nucleus would not meaningfully impact its fusion probability.

Table 1. Comparison of the total electron energy level in zitterbewegung orbit state around various nuclei.

Nucleus	Potential energy (keV)	Kinetic energy (keV)	Total electron energy (eV)
^{1}H	–3.756	3.837	81
^{2}H	–3.756	3.791	35
^{7}Li	–11.44	11.59	150

3.2. Transition to close electron–nucleus proximity state

Since the use of heavier elements for catalyzing electron transition into zitterbewegung orbit was documented in [18], we consider the possibility that the initiating electron kinetic energy for the above-described meta-stable state does not need to come from a free electron, but it may be the kinetic energy of a bound electron's orbit. Specifically, a bound electron of some heavier atom may transition into an electron–proton or electron–deuteron zitterbewegung orbit state when its wavefunction overlaps with an approaching proton or deuteron nucleus. The virial theorem states that in a single electron hydrogen atom the electron's kinetic energy is equal to its ionization energy. In multi-electron atoms this relationship may not be exact, but nevertheless we can use the electron ionization energy to estimate its kinetic energy. Table 2 lists the estimated electron ionization energies for nickel's outer electrons. For the outermost N1

Table 2. Listing of electron ionization energies in nickel's outer orbitals.

Orbital	N1	M5	M4	**M3**	M2	M1
Ionization energy (eV)	7.64	15	15.7	**79**	84.2	124.4

electron orbital, we used the available ionization energy data. For the other electrons, we accounted the relative X-ray transition energies between the N1 and other orbitals, and added the ionization energy of the N1 orbital.

Visible light driven transmutation in the presence of a bromine-containing catalyst (Eosin-Y) was reported in [17]. Since nickel and bromine both appear to be initiating catalysts of nuclear reactions, we compare their electron energy levels. The ionisation energy of bromine's electrons in the brominated organic compound can be estimated to be the similar as in the atomic bromine. Comparing data of Tables 2 and 3, the common energy level appears to be at 79–80 eV. Since [17] reports visible light driven transmutation, the electron kinetic energy for zitterbewegung orbit transition is within 1–2 eV from this common 79–80 eV level. We note the very good match between this 80 eV energy level and its theoretic estimation in Section 3.1.

Table 3. Listing of electron ionization energies in bromine's outer orbitals.

Orbital	N3	N2	N1	M5	**M4**	M3	M2	M1
Ionization energy (eV)	12.5	11.8	23.5	78.3	**79.4**	191.2	198.5	264.8

Using the same methodology, we calculated the electron kinetic energies of other elements around nickel. As seen in Fig. 12, there are several elements which have close to 80 eV kinetic electron energy level. However, elements with more than than 80 eV of electron energy, such as Cr or Cu, may not be suitable if their kinetic energy is slightly excessive with respect to the resonant transition energy level. Besides Ni and Br, at least Co and V are expected to have suitable electron energy level.

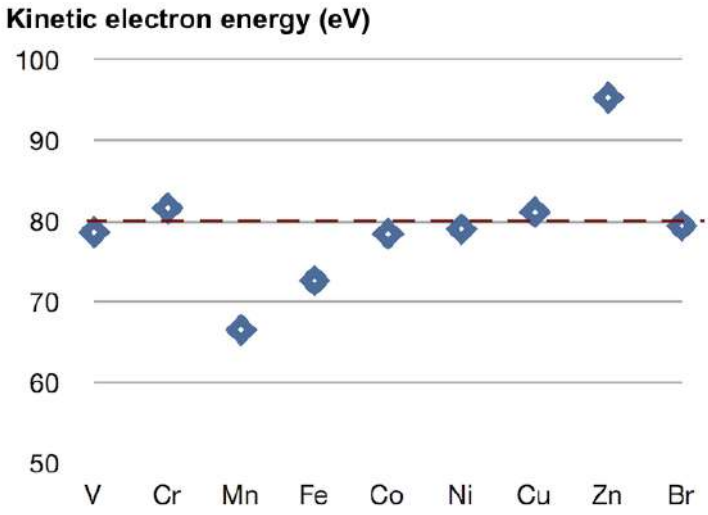

Figure 12. Display of electron energies which are closest to the 80 eV level, shown for elements around Ni.

By comparing Refs. [3] and [5], we observe an important distinction between hydrogen and deuterium fuels: while a nickel-based reactor produces exothermic energy with hydrogen fuel, it only produces exothermic energy with deuterium fuel after applying a palladium surface coating over it. This experimental evidence supports the above identified hydrogen vs. deuterium difference in the electron transition energies. Reference [28] reports nuclear transmutation effects initiated upon passing deuterium through thin CaO layers. These findings were replicated in [29], and its authors also clarified that such transmutations do not occur with with hydrogen gas, but only with deuterium gas. As seen in Table 4, calcium indeed contains approximately 35 eV electron kinetic energy orbitals. According to [30], the M1 orbital's electron binding energy is 0.6 eV higher in CaO than in metallic Ca. Assuming similar energy shift also for the other M-orbitals, in CaO we estimate the M2 and M3 orbitals' kinetic energy levels at 35.6 and 35.1 eV, respectively, in good agreement with our theoretical prediction.

Table 4. Listing of electron ionization energies in calcium's outer orbitals.

Orbital	N1	**M3**	**M2**	M1
Ionization energy (eV)	6.1	**34.6**	**35**	55.5

We make the following proposition about the transition to the close electron–nucleus proximity state: (i) A transition into zitterbewegung orbit around a proton occurs at the 80 eV electron kinetic energy level, and at 35 eV in case of a deuteron; (ii) The electrons of interest are those which have only a small gap with respect to the required energy level – however these are chemically inactive inner electrons. 1–10 eV energy range collisions between atoms can energize such inner electrons of interest to the transition energy level.

The required 1–10 eV collision energy is higher than what can be normally supplied by thermal heating. However, such collision energy may be supplied by a Fermi potential difference between interfaces, by an applied electric field in an electrolysis setup, or by energetic plasmon oscillations. In [21], accelerated uranium decay was observed when aqueous solution of uranium ions was subjected to laser induced plasmons on gold surface. In that study, the measured plasmon energy was over 5 eV. The most plausible explanation involves the above outlined process, resulting in one of gold's or uranium's electrons to be energized to the right kinetic energy level for the transition into a highly localized electron orbit around the H or D nucleus of the water solvent. Some of these resulting quasi-neutron-like particles accelerate uranium's decay by fusing into the uranium nucleus. Such intermediating role of the H or D nucleus is proved by the varying decay rates observed in H_2O vs. D_2O solution.

3.3. Experimental conditions for the transition process

On the basis of the above outlined electron transition process, this section analyzes collisions between atoms in those experimental setups where continuous energy production has been observed. The analysis of Ni–Li phase diagram reveals that Li alloys with Ni up to 10–15 atomic%, above which ratio there are two immiscible phases: an Ni-rich and a Li-rich phase. Similarly, the Cu–Li phase diagram indicates that Cu has a very low alloying capability with Li. Therefore, in our Li–Ni–Cu fueled experiments there is a phase boundary between the molten Li rich and the solid Cu/Ni rich phases. The Fermi level difference between these two phases is estimated to be 5–7 V. Figure 13 illustrates this electronic structure and the influx of cations into the accelerating boundary region during melting. Since Cu and Ni are +2 charged in the metallic environment, the ions crossing over the molten-solid phase boundary during melting process gain 10-14 eV on the average, accelerated by the electric field between these two phases. Their subsequent collision with ions in the molten phase produces the condition allowing the transition of some inner electron into close proximity zitterbewegung orbit. In other words, some fraction of these accelerated ions' kinetic energy provides the missing electron energy for the highly localized transition. Since the Constantan alloy has a continuous melting

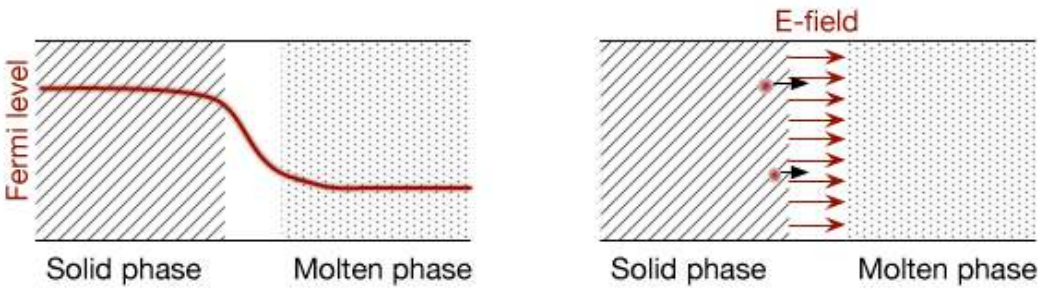

Figure 13. Illustration of the Fermi level difference between solid/molten phases in our experiment (*left*) and the ion flux into the accelerating region during melting (*right*.)

temperature range between 1250 and 1300°C, the continuous acceleration of ions during the heating phase may explain the apparently constant reaction power during the heating phase. There is no similar ion accelerating process during the cooling phase; this difference corresponds to the observed approximately zero reaction power during the cooling phase.

The role of the surface interface has also been reported in hydrogenated/deuterated Ni experiments. In [2], the authors reported the exothermic reaction power to be related to the surface area size of the interface between hydrogenated constantan and borosilicate fiberglass. In [3], the authors reported the exothermic reaction power to require the presence of deuterated nickel – palladium interface. Such interfaces are needed for creating a Fermi level difference between two solid state materials in physical contact. While there is no molten phase in these experiments, H^+ or D^+ ions may be diffusing across such interface, and thereupon being accelerated by the electric field counter-balancing to the Fermi level difference. Indeed, the authors of [2] noted the adsorption of hydrogen on the surface of fiberglass, and the authors of [3] used palladium which has a high hydrogen absorption. These choices of surface layer materials set up the condition for H^+ or D^+ ions diffusing across an interface involving a Fermi level difference. The exothermic reaction power should be therefore proportional to the H^+ or D^+ diffusion rate, which is related to the temperature by the $\exp\left(-E_a/k_B T\right)$ factor, where E_a is the activation energy for diffusion. As shown in Fig. 14, the exponential power dependence on the reactor temperature was indeed confirmed in [3].

Altogether, the concept of electron transition to highly localized zitterbewegung orbit appears to be a useful starting point for explaining the experimental observations. In various experiments, the observed reaction dynamics matches the proposed trigger condition of 1–10 eV range excitations. Identifying the details of the consequent electron mediation enabled nuclear processes requires further study. This analysis points to the role of hydrogen in our experimental setup. This suspected role of hydrogen will be validated in future replications of the experiments described in [4], where the fuel containers shall be assembled and sealed under inert gas atmosphere.

3.4. Production of highly localized electrons by braking energetic particles

The rate of p or D involving nuclear fusion reactions has been extensively studied in various materials. The fusion enhancement rate is generally characterized by the screening energy parameter U_e, characterizing the fusion rate enhancement over a range of incoming ion beam energies. Up to now, the observed fusion rate enhancement was generally thought to be a consequence of delocalized electron screening, which is described by the Thomas–Fermi screening model.

Table 5 shows the screening energy parameter in various background materials of interest, from data reported in [12,14,15]. A very strong fusion enhancement is seen in hydrogenated graphite; in this environment the 5.6 MeV

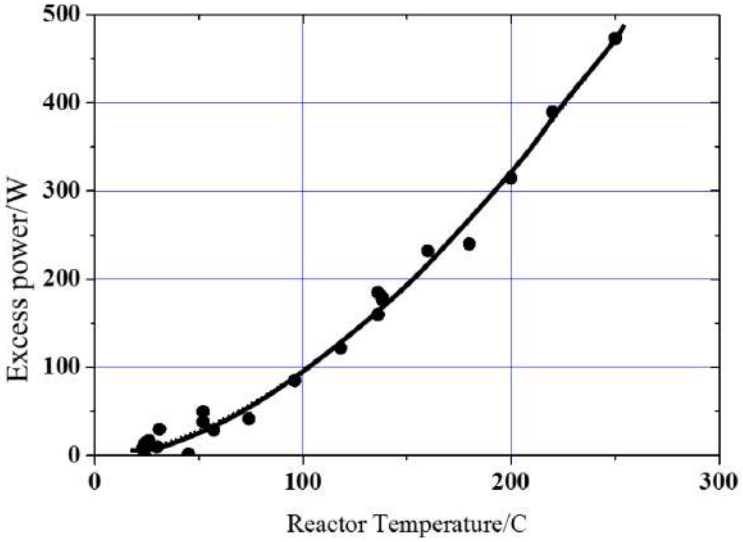

Figure 14. The exponential temperature dependence of excess reaction power in a solid-state deuterated Ni fuel, reproduced from [3].

Table 5. Fusion rate enhancement characterized by the screening energy parameter for the p+^{7}Li (A), D+^{6}Li (B), and p+^{19}F (C) reactions.

	Material	H stoichiometry	U_e
	TiH	1.03	3.9 keV
A	$PdH_{0.2}$	0.21	3.6 keV
	Graphite	0.06	10.3 keV
	LiF		350 eV
B	Solid Li		400 eV
	Liquid Li		700 eV
	Kapton		0 keV
C	Amorphous carbon (hydrogenated)		36 keV
	TiH		73 keV
	Graphite (hydrogenated)		115 keV

electron-assisted nuclear de-excitation has been also observed. Strong fusion rate enhancements are observed for hydrogenated Ti and Pd materials, and by analogy it is reasonable to expect hydrogenated Ni to also have similar screening energy parameter.

A significantly higher fusion rate enhancement is seen in molten lithium than in solid lithium or lithium fluoride. Interestingly, this liquid phase rate enhancement appears to be specific to lithium, and not a general solid-liquid difference in metals. In related experiments [12,13], the authors performed deuterium bombardment of solid/molten indium and ^{6}Li metals respectively. These studies show that at 10 keV bombardment, the reaction rate is about two orders of magnitude higher in solid indium than in liquid indium. In contrast, the reaction rate has been about 40% higher in liquid lithium than in solid lithium.

Altogether, the screening energy data shows several major inconsistencies with the delocalized electron screening

model. (i) The fusion rate enhancement is 3–4 orders of magnitude higher in some cases, e.g. in hydrogenated graphite, than the theoretically predicted Thomas–Fermi screening model based screening energy parameter. (ii) The solid–liquid phase transition has strong influence on the screening energy, which is unexpected. (iii) The chart of the fusion rate vs. ion beam energy deviates from the theoretically expected chart. The analysis of this deviation prompted the authors of [20] to suggest a "nuclear reaction resonance" at 105 ± 15 eV. Perhaps coincidentally, such 105 eV resonant ion energy implies 105/3=35 eV average kinetic energy along each spacial axis during its deceleration, which is matching the 35 eV kinetic electron energy required for the establishment of zitterbewegung orbit around D nucleus.

When the fusion reaction involves p or D, any highly localized electrons around the p or D nuclei increase the probability of fusion between these screened p or D and other nuclei. Therefore, measuring the fusion enhancement rate is also a suitable proxy for measuring the production rate of such highly localized zitterbewegung orbit electrons. The correspondence between the observation of surprisingly strong screening energy parameter in graphite and the observation of electron-assisted nuclear de-excitation indicates that the screening energy parameter may in fact measure the rate of highly localized electron production. At a given proton beam energy, the theoretical rate of p+^{7}Li fusion is much higher than the rate of p +^{19}F fusion due to the Coulomb barrier difference. Since the rate of highly localized electron production in a given material is the same in either case, the apparent screening energy parameter becomes an order of magnitude higher for the p +^{19}F fusion case, as seen in the data of Table 5.

Based on the above discussed transition model, the production of highly localized electrons around a proton may happen via direct excitation of delocalized electrons to 80 eV kinetic energy or via the small excitation of those bound electrons which have already close to 80 eV kinetic energy. In case of a deuteron nucleus, this energy level is 35 eV.

While the 105 ± 15 eV resonance proposed in [20] is too low value for any conceivable nuclear process, it is indicative of the required electron kinetic energy level for transition into highly localized state, assuming a thermalization type coupling between kinetic ion energy and electron excitation at similar energy. While in metals the electronic excitation lifetime is proportional to the inverse square of the excitation energy, in graphite the electronic excitation lifetime is proportional to the inverse of the excitation energy [24]. This property of graphite may explain the higher screening energy parameter in the graphite environment.

Regarding the excitation of already close to 35 eV inner electrons, Refs. [22,23] provide insightful data. Reference [22] reports 600 eV screening energy for D–D fusion in PdO, in contrast to the 300 eV screening energy for Pd, measured using the same methods. This is again contrary to the Thomas–Fermi screening model, which predicts a higher screening energy parameter for the delocalized electron containing Pd. We estimate the kinetic energies of palladium's orbitals, and surprisingly find that none of them are in the proximity of 35 eV. This points to the possibility that oxygen's L1 orbital may be near 35 eV, at some locations of PdO. According to [30], oxygen's L1 orbital kinetic energy is varying in the wide range of 12 eV, depending on oxygen's oxidation state. Reference [23] shows that in Zr environment the D–D fusion enhancement factor varies with the amount of Zr surface oxidation. This dependence is shown in Fig. 15. For zirconium, we also find that none of its orbitals are in the proximity of 35 eV. Therefore, palladium-oxide and zirconium-oxide involving experiments reveal that oxygen appears to be the common source of fusion enhancement. However, since the fusion enhancement peaks at a certain level of surface oxidation, it is not the fully oxidized state of zirconium surface where oxygen's L1 orbital energy has close to 35 eV kinetic energy. We suggest that there may be an uncommon oxidation state where oxygen's L1 orbital energy is close to 35 eV, and such uncommon oxygen state may be present at the "nuclear active environment" sites. Several researchers of palladium–deuterium reactors suggest the so-called "nuclear active environment" surface sites to be the active spots where nuclear reactions occur.

In summary, measurements of the screening energy parameter show results which are incompatible with the delocalized electron screening concept and appear to be quantifying the production rate of highly localized zitterbewegung orbit electrons by energetic particles. The data shows that the kinetic energy for such meta-stable state initiation may indeed originate either from a delocalized electron energized to 80 eV or 35 eV, or from a similar kinetic energy of

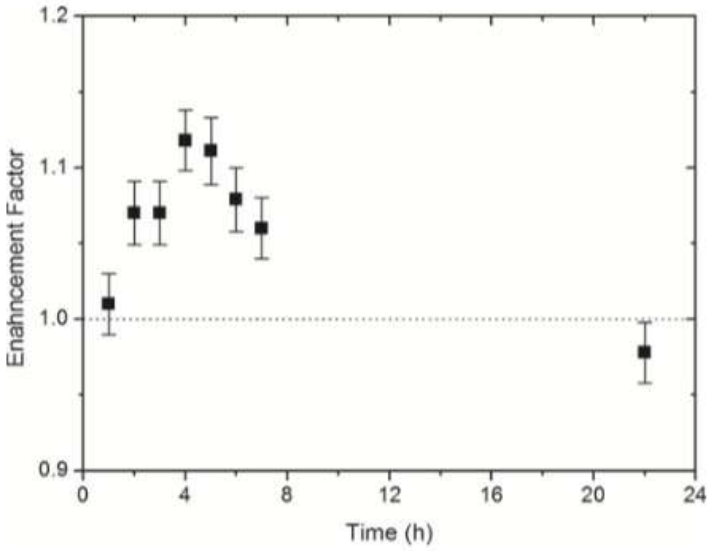

Figure 15. The D–D fusion enhancement factor measured for 15 keV deuteron bombardment of Zr, reproduced from [23]. The chart is showing the enhancement evolution with respect to the initial fusion rate. The Zr surface is oxidation-free at the start of experiment, and oxidizes gradually.

a bound electron's orbit. The previously overlooked role of oxygen in deuterium-fueled experiments is pointed out. We note that Tables 2–4 relate to experiments demonstrating nuclear energy production and transmutation; i.e. the identified energy level is derived from a broad base of diverse experiments.

The possibility of a positive feedback loop between the energetic electrons produced by a nuclear reaction and the production of more highly localized electrons during the braking of these energetic electrons explains the burst-like reaction dynamics, which was experimentally observed.

3.5. Quantitative predictions

If a physical process model is valid, it must be possible to derive refutable predictions from it. Such predictions are specific to the model, and the proposed process may be proven correct by the validation of these predictions. In this section we therefore make a number of quantitative predictions which are unique to the electron mediated nuclear reaction model described herein, and which may be used for its validation:

(1) **Observable signatures at 35 eV or 80 eV electron kinetic energy**. The most important prediction is the above explained role of the 80 eV energy level in hydrogen fueled reactors and 35 eV energy level in deuterium fueled reactors. We predict that various other transition signatures shall be found at these electron kinetic energy levels. Specifically, we predict that the "runaway electron" production of hot fusion reactors is a signature of this phenomenon. It has been known for over 40 years that hot plasmas occasionally enter into a state characterized by emission of energetic electrons and concurrent enhanced neutron emission. Such state tends to appear during the disruption or shutdown of the hot plasma current. The so-called "Dreicer mechanism", which most related publications mention as a proposed explanation for this phenomenon, is contrary to the basic principles of plasma physics and thermodynamics. Figure 16 shows the appearance of a "runaway current

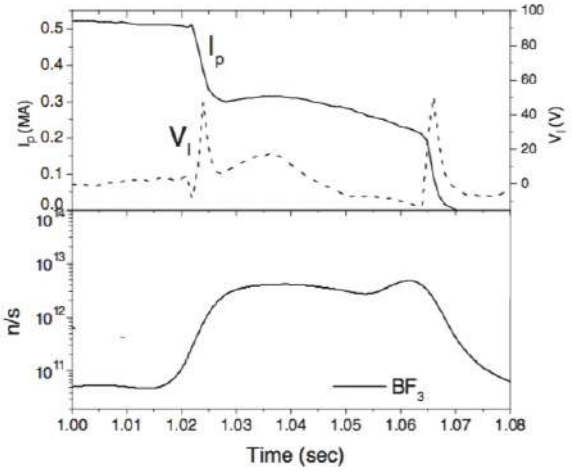

Figure 16. Energetic electron production in a tokamak reactor during a post-disruption current plateau, reproduced from [25]. I_P indicates the plasma current, V_I indicates the tokamak loop voltage, and the bottom part shows the amount of neutrons measured by a BF_3 detector. The plasma disruption takes place at about 1.02 s. We predict approximately 35 eV electron temperature during such current plateau.

plateau", which suddenly appears after a thermal cooling phase, and whose duration coincides with the neutron production process. The appearance of such current plateau is unexpected and unexplained in the context of the "Dreicer mechanism" theory. We predict that the electron temperature in such a "runaway current plateau" shall be eventually measured to be close to 35 eV, and that the nuclear origin of the energetic electrons shall be recognized. In [25], the authors estimate the electron temperature during runaway current plateaus to be 42 eV, based on the current evolution characteristics. This indirect estimation is fairly close to the 35 eV electron temperature predicted by us.

(2) **690 THz radiation signature of proton-electron zitterbewegung orbit establishment and 212 THz radiation signature of deuteron–electron zitterbewegung orbit establishment**. The proposed magnetic stabilization of zitterbewegung orbit states implies nuclear Zeeman level splitting, analogously to the resonance exploited nuclear magnetic resonance imaging devices. For the proton-electron system, we predict visible photon emission near the 690 THz frequency level upon the meta-stable zitterbewegung orbit establishment. This prediction is based on the calculation of magnetic field strength at the center of zitterbewegung orbit [10]. For the deuteron-electron system, we predict 212 THz emission, which is in the near-infrared range. Reference [31] indeed reports unexplained non-thermal near-infrared emission in a deuterium electrolysis based experiment, and mentions several other experiments documenting the same phenomenon. The intensity of the emission was found to be correlated with the measured non-chemical power output, which demonstrates that the zitterbewegung orbit electron state catalyzes nuclear reactions. An interesting point about this prediction is that an accurate measurement of the predicted frequency reveals the exact magnetic field strength at the center of the zitterbewegung orbit. As far as we know, no experiment measured yet the frequency of this photon emission.

(3) **Metastable hydrogen molecule with picometer-range internuclei distance**. Consequent to the zitterbewegung orbit's magnetic moment, two proton–electron systems in zitterbewegung orbit state shall experience magnetic attraction, and shall assume the energetically most favorable stacked orbit orientation. This prediction appears to be validated by the 2.3 pm inter-nuclei distance measurement reported in [18], which corresponds

to the theoretically expected inter-nuclei distance discussed in [10].

(4) **Energetic electron emission with energies up to the nuclear reaction energy**. We predict that the zitterbewegung orbit catalyzed nuclear reactions emit energetic electrons. Specifically, the energy of emitted electrons may reach up to the nuclear reaction energy level, i.e. 5.6 MeV for p-D fusion and 24 MeV for D–D fusion. For p-D fusion, this prediction is compatible with the observation of 5.6 MeV electron energy [7], and for D-D fusion this prediction is compatible with the observation of up to 15 MeV electron energies [26], where the upper energy threshold was limited by the sensitivity of the detecting equipment. It requires further study to understand why such electron emission is apparently high in burst type reactions and low in continuous reactions.

4. Conclusions

We have shown that the exothermic nuclear reaction in nickel-fueled reactors appears to be electron-mediated. We observe the distinct reaction dynamics of a fast burst and a continuous reaction process. Apparently, these are two different nuclear reaction processes. The analysis of the continuous reaction dynamics shows its highly controllable characteristics. This controllable characteristic, its high 30 W/g reaction power rate, and the reliable reaction start-up in our experimental design imply great potential for future energy production. We constructed a theory to explain the experimental observations in nickel-involving nuclear experiments; this theory builds onto previous works of relativistic electron dynamics. This model leads us to propose the presence of highly localized electron states, which are in close nuclear proximity around a proton or deuteron, and related experimental evidence for such close-proximity electron-nucleus configuration has been reviewed. The initiating electron kinetic energy level of 80 eV for hydrogen and 35 eV for deuterium are identified from experimental data, which is in good agreement with our theoretical estimation. The proposed transition process into highly localized electron states matches well the observed reaction data, and we described this process in sufficient detail for guiding future experimental work. This theory may be therefore useful for validation experiments and optimized reactor designs. The theory of zitterbewegung orbit state and its relation to the Dirac equation are described in more detail in a forthcoming book titled: "*Maxwell–Dirac Theory and Occam's Razor: Unified Field, Elementary Particles and Nuclear Interactions*".

Acknowledgments

We thank Serge F. Timashev, Jirohta Kasagi, and Pekka Janhunen for insightful discussions, and Kimmo Lattu for helping with the reactor preparation.

References

[1] J. Kasagi, T. Itoh and Y. Iwamura, Search for γ-ray radiation in NiCuZr nano-metals and H_2 gas system generating large excess heat, *Proc. ICCF-21 Int. Conf. on Condensed Matter Nucl. Sci.*, Fort Collins, USA, 2018.

[2] F. Celani, A. Spallone, B. Ortenzi, S. Pella, E. Purchi, F. Santandrea, S. Fiorilla, A. Nuvoli, M. Nakamura, P. Cirilli, P. Boccanera and L. Notargiacomo, Observation of macroscopic current and thermal anomalies, at high temperature, by hetero-structures in thin and long constantan wires under H_2 gas, *J. Condensed Matter Nucl. Sci.* **19** (2016) 29–45.

[3] T. Mizuno, Observation of excess heat by activated metal and deuterium gas, *J. Condensed Matter Nucl. Sci.* **25** (2017) 1–25.

[4] A. Kovacs, D. Brown and F. Ek, Exothermic reactions in the partially molten Li–Ni–Cu alloy, *J. Condensed Matter Nucl. Sci.* **25** (2017) 159–180.

[5] S. Focardi, V. Gabbani, V. Montalbano, F. Piantelli, S. Veronesi, Evidence of electromagnetic radiation from Ni–H Systems, *Proc. ICCF-11 Int. Conf. on Condensed Matter Nucl. Sci.*, Marseille, France, 2004.

[6] M. Valat, A. Goldwater, R. Greenyer, R. Higgins and R. Hunt, Investigations of the Lugano HotCat reactor, *J. Condensed Matter Nucl. Sci.* **21** (2016) 81–96.
[7] M. Lipoglavsek, S. Markelj, M. Mihovilovič, T. Petrovič, S. Itajner, M. Vencelj, J. Vesič , Observations of electron emission in the nuclear reaction between protons and deuterons, *Phys. Lett.* B **773** (10) (2017) 553–556, DOI:10.1016/j.physletb.2017.09.004.
[8] A. Takahashi, A. Kitamura, R. Seto, Y. Fujita, Taniike, Y. Furuyama, T. Murota and T. Tahara, Anomalous exothermic and endothermic data observed by nano-Ni-composite samples, *J. Condensed Matter Nucl. Sci.* **19** (2016) 23–32.
[9] T. Ohtsuki, K. Ohno, T. Morisato, T. Mitsugashira, K. Hirose, H. Yuki and J. Kasagi, Enhanced electron-capture decay rate of ^{7}Be encapsulated in C_{60} cages, *Phy. Rev. Lett.* **93** (11) (2004).
[10] F. Celani, A. O. Di Tommaso and G. Vassallo, The electron and occam's razor, *J. Condensed Matter Nucl. Sci.* **25** (2017) 76–99.
[11] T.A. Góngora and R.G. Stuart, The charge radius and anapole moment of a free fermion, *Zeitschrift für Physik* C – *Particles and Fields* **55** (1) (1992) 101–105.
[12] J. Kasagi, Screening potential for nuclear reactions in condensed matter, *Proc. ICCF-14 Int. Conf. on Condensed Matter Nucl. Sci.*, Washington, DC, 2008.
[13] J. Kasagi and Y. Honda, Screening energy of the d+d reaction in an electron plasma deduced from cooperative colliding reaction, *J. Condensed Matter Nucl. Sci.* **19** (2016) 127–134.
[14] A. Cvetinovic, M. Lipoglavëk, S. Markelj, J. Vesič, Molecular screening in nuclear reactions, *Phy. Rev.* C **92** (6) (2015).
[15] M. Lipoglavsek, Catalysis of nuclear reactions by electrons, EPJ Web of Conferences, Vol. 165, 2017.
[16] Y. Iwamura, T. Itoh, J. Kasagi, A. Kitamura, A. Takahashi and K. Takahashi, Replication experiments at tohoku university on anomalous heat generation using nickel-based binary nanocomposites and hydrogen isotope gas, *J. Condensed Matter Nucl. Sci.* **24** (2017) 191–201.
[17] G. Lu and W. Zhang, Photocatalytic hydrogen evolution and induced transmutation of potasium to calcium via low energy nuclear reaction (LENR) driven by visible light, *J. Mol. Catalysis* **31** (5) (2017) 401–410.
[18] S. Zeiner-Gundersen, Hydrogen reactor for rydberg matter and ultra dense hydrogen, a replication of Leif Holmlid, presentation at the ICCF-21 conference, Fort-Collins, USA, 2018.
[19] G.H. Miley and J.A. Patterson, Nuclear transmutations in thin-film nickel coatings undergoing electrolysis, *J. New Energy* **1** (3) (1996).
[20] M. Kaczmarski, K. Czerski, D. Weissbach, A. Huke, G. Ruprecht and A. I. Kilic, Threshold resonance contribution to the thick target ^{2}H(d,p)^{3}H reaction yield, *Acta Physica Polonica* B, **48** (3) (2017) 489–493.
[21] A.V. Simakin and G.A. Shafeev, Accelerated alpha decay under laser exposure of metallic nanoparticles in aqueous solutions of uranium salt, *Phys. Wave Phenomena* **19** (1) (2011) 30–38.
[22] J. Kasagi, Low-energy nuclear reactions in metals, *Progr. Theoret. Phys. Supplement* **154** (1) (2004) 365–372.
[23] K. Czerski, D. Weissbach, A.I. Kilic, G. Ruprecht, A. Huke, M. Kaczmarski, N. Targosz-Ślęczka and K. Maass, Screening and resonance enhancements of the ^{2}H(d,p)^{3}H reaction yield in metallic environments, *Europhys. Lett.* **113** (2) (2006).
[24] S. Xu, J. Cao, C.C. Miller, D.A. Mantell, R.J.D. Miller and Y. Gao, Energy dependence of electron lifetime in graphite observed with femtosecond photoemission spectroscopy, *Phy. Rev. Lett.* **76** (3) (1996) 483–486.
[25] J.R. Martin-Solis, B. Esposito, R. Sánchez, F.M. Poli and L. Panaccione, Enhanced production of runaway electrons during a disruptive termination of discharges heated with lower hybrid power in the Frascati Tokamak Upgrade, *Phy. Rev. Lett.* **97** (16) (2006).
[26] C. Paz-Soldan, C.M. Cooper, P. Aleynikov, D.C. Pace, N.W. Eidietis, D.P. Brennan, R.S. Granetz, E.M. Hollmann, C. Liu, A. Lvovskiy and R.A. Moyer, Spatiotemporal evolution of runaway electron momentum distributions in tokamaks, *Phy. Rev. Lett.* **118** (25) (2017).
[27] P. Kálmán and T. Keszthelyi, Solid state internal conversion, *Phy. Rev.* C **69** (3) (2004).
[28] Y. Iwamura, M. Sakano and T. Itoh, Elemental analysis of Pd complexes: effects of D_2 gas permeation, *Japanese J. Appl. Phys.* **41** (7R) (2002).
[29] T. Hioki, N. Takahashi, S. Kosaka, T. Nishi, H. Azuma, S. Hibi, Y. Higuchi, A. Murase and T. Motohiro, Inductively coupled plasma mass spectrometry study on the increase in the amount of Pratoms for Cs-ion-implanted Pd/CaO Multilayer complex with deuterium permeation, *Japanese J. Appl. Phys.* **52** (10R) (2013).

[30] NIST X-ray photoelectron spectroscopy database, https://srdata.nist.gov/xps.
[31] M. Swartz, G. Verner and A. Weinberg, Non-thermal near-IR emission from high impedance and codeposition LANR devices, *Proc. ICCF-14 Int. Conf. on Condensed Matter Nucl. Sci.*, Washington, DC, 2008.